CHALMERS

Chalmers Publication Library

Molecular-line and continuum study of the W40 cloud

(article starts on next page)

Molecular-line and continuum study of the W40 cloud

L. Pirogov,[1]⋆ D. K. Ojha,[2] M. Thomasson,[3] Y-F. Wu[4] and I. Zinchenko[1]

[1]*Institute of Applied Physics RAS, Ulyanova 46, Nizhny Novgorod 603950, Russia*
[2]*Department of Astronomy and Astrophysics, Tata Institute of Fundamental Research, Homi Bhabha Road, Mumbai 400005, India*
[3]*Chalmers University of Technology, Department of Radio and Space Science, Onsala Space Observatory, SE-43992 Onsala, Sweden*
[4]*Department of Astronomy, School of Physics, Peking University, Beijing, 100871, China*

ABSTRACT

The dense cloud associated with W40, which is one of the nearby H II regions, has been studied in millimetre-wave molecular lines and in the 1.2-mm continuum. Moreover, 1280- and 610-MHz interferometric observations have been carried out. The cloud has a complex morphological and kinematical structure, including a clumpy dust ring and an extended dense core. The ring has probably been formed by the 'collect and collapse' process as a result of the expansion of the neighbouring H II region. Nine dust clumps in the ring have been deconvolved. Their sizes, masses and peak hydrogen column densities are $\sim$0.02–0.11 pc, $\sim$0.4–8.1 $M_\odot$ and $\sim$(2.5–11) $\times$ 10^{22} cm^{-2}, respectively. Molecular lines are observed at two different velocities and have different spatial distributions, which implies that there is strong chemical differentiation over the region. The CS abundance is enhanced towards the eastern dust clump 2, while the NH_3, N_2H^+ and $H^{13}CO^+$ abundances are enhanced towards the western clumps. HCN and HCO$^+$ do not correlate with the dust, probably tracing the surrounding gas. The number densities derived towards selected positions are $\sim$(0.3–3.2) $\times$ 10^6 cm^{-3}. The two western clumps have kinetic temperatures of 21 and 16 K and are close to virial equilibrium. The eastern clumps 2 and 3 are more massive, have a higher extent of turbulence and are probably more evolved than the western clumps. They show asymmetric CS(2–1) line profiles because of infalling motions, which is confirmed by model calculations. An interaction between ionized and neutral material is taking place in the vicinity of the eastern branch of the ring and probably triggers star formation.

Key words: stars: formation – ISM: clouds – ISM: individual objects: W40 – ISM: molecules – radio continuum: ISM.

1 INTRODUCTION

The process of high-mass star formation attracts much attention nowadays. There is still no general theory of high-mass star formation and evolution (e.g. Zinnecker & Yorke 2007) as in the case of low-mass star formation. The regions where massive stars are forming are more rare, more distant and evolve more quickly than low-mass star-forming regions. During their evolution, massive stars affect the surrounding parent cloud as a result of stellar winds, massive outflows, strong ultraviolet radiation and the expansion of H II regions. These strong impacts affect the physical conditions and chemical composition of the parent cloud and might cause contraction and trigger the formation of a new generation of stars. Therefore, detailed studies of high-mass star-forming (HMSF) regions are important.

One of the nearby regions of high-mass star formation, W40, which is also known as Sharpless 64 (Westerhout 1958; Sharpless

1959), contains a large blister-type H II region ($\sim$1 pc in diameter) that lies at the edge of an extended molecular core (TGU 279-P7, according to Dobashi et al. 2005) in the Aquila Rift complex at the Galactic latitude $b \sim 3°\!.5$. The region has been extensively studied at different wavelengths. There is an embedded cluster of young stars in the centre of the region. Rodney & Reipurth (2008) have given a review of the existing data and the properties of the H II region, the inner sources and the molecular cloud. More recent observational data of the region are obtained in the radio (Rodríguez, Rodney & Reipurth 2010), near-infrared (NIR; Shuping et al. 2012) and X-ray (Kuhn et al. 2010) ranges. The Aquila Rift complex, including the W40 region, has been observed in the millimetre continuum by Maury et al. (2011). On the basis of original and archival multiwavelength data, Mallick et al. (2013) have recently conducted a survey of W40 on large scales.

The distance to the W40 region is not exactly constrained. Atomic and molecular-line observations have enabled us to deduce a kinematical distance of 600 ± 300 pc (Radhakrishnan et al. 1972; see also discussions by Vallée 1987; Rodney & Reipurth 2008). The far

⋆ E-mail: pirogov@appl.sci-nnov.ru

Table 1. Parameters of the single-dish molecular-line observations.

Telescope	Frequency (GHz)	$\Delta\Theta$ (arcsec)	η_{mb}	T_{sys} (K)	δV (km s^{-1})
IRAM-30	85–99	29–26	∼0.8	110–140	0.24–0.27
	245	10	∼0.57	400–600	0.38
OSO-20	86–96	∼ 40–44	∼ 0.38–0.45	200–700	0.078–0.087
Effelsberg-100	23.7	40	0.53	70–110	0.039

value of the twofold ambiguity in the kinematical distance calculations is rejected on the basis of optical identification and the high distance from the Galactic plane (Reifenstein et al. 1970). Bontemps et al. (2010) have associated W40 with the Serpens star-forming region in the Aquila Rift complex and have suggested a distance of 260 pc. Kuhn et al. (2010) have used the X-ray luminosity function (XLF) fitting method and have derived a best-fitting distance value of 600 pc. Recently, from an analysis of NIR data, Shuping et al. (2012) have estimated that the distance to three stars of the W40 cluster is between 455 and 536 pc. They have ruled out distances less than 340 pc and higher than 686 pc. We adopt a distance of 500 pc throughout our paper. This puts W40 among the most closely located HMSF regions.

The associated W40 molecular cloud is located ∼2 arcmin to the west of the H II region. This has been observed in molecular and atomic lines by different authors. Early CO(1–0) observations by Zeilik & Lada (1978) revealed a region of extended emission at ∼4.5 km s^{-1}, with two emission peaks located in the north–south direction. They argued that the velocity difference between the CO and hydrogen recombination lines (∼4 km s^{-1}) is consistent with the blister model in which the H II region lies at the front edge of the cloud closer to the observer. Based on the carbon recombination-line observations at ∼6.5 km s^{-1}, Vallée (1987) has proposed a model according to which the western portion of the H II region is obscured by a molecular cloud. Crutcher (1977) observed the OH absorption lines at ∼7 km s^{-1} towards the W40 H II region. The molecular cloud was mapped in CO, ^{13}CO, HCO$^+$, HCN and Hα by Crutcher & Chu (1982). They have revealed that the CO and ^{13}CO line profiles possess two emission features at ∼5 and ∼8 km s^{-1}. These two velocity components have different spatial distributions. The HCN and HCO$^+$ maps reveal the existence of a high-density core. The HCO$^+$(1–0) linewidths (∼1.4 km s^{-1}; Pirogov et al. 1995) imply that there is a moderate degree of turbulence of the dense gas compared with typical HMSF regions (Pirogov et al. 2003). The CO isotopic line observations by Zhu, Wu & Wei (2006) allow us to determine the mass of the W40 core ∼200–300 M$_\odot$, which is close to model estimates from Vallée, Guilloteau & MacLeod (1992) and typical for HMSF cores. Weak CO outflow has been detected in the centre of the core by Zhu et al. (2006), but the driving source of the outflow remains undiscovered. Mallick et al. (2013) have derived a lower limit on the mass contained within the area of the 3-arcmin radius around the central sources of 126 M$_\odot$.

Our goal is to study the structure of the W40 cloud in the vicinity of the H II region where interaction between ionized and dense neutral material is taking place. It is important to derive the gas and dust physical parameters as well as the chemical composition of the gas, where formation of the next generation of stars is probably taking place.

2 OBSERVATIONS

We performed molecular multiline and dust continuum observations of the W40 cloud at millimetre wavelengths using the IRAM-30,

Onsala-20 and Effelsberg-100 telescopes. The region was also observed at 1280 and 610 MHz (UHF band) with the Giant Metrewave Radio Telescope (GMRT) array. Our maps are centred at the position RA (J2000) = 18^{h}31^{m}15^{s}75, Dec. (J2000) = −02°06′49″3, which is close to the CO and ^{13}CO peak positions from Zhu et al. (2006). The parameters of single-dish molecular-line observations are given in Table 1.

2.1 IRAM-30 observations

Mapping of the W40 cloud in the CS(2–1), CS(5–4), N$_2$H$^+$(1–0) and CH$_3$CCH(5–4) molecular lines was performed in 2010 August at the IRAM-30 telescope with the Eight Mixer Receiver (EMIR; E090/E230 bands combination). The Vespa autocorrelator with 0.08 and 0.32 MHz spectral resolutions for the E090 and E230 bands, respectively, was used as a backend. In addition, the Wilma auto-correlator with 2-MHz spectral resolution was used. The maps were taken in the on-the-fly (OTF) mode and covered a 6 × 4 arcmin^2 region around the central position; the region observed in N$_2$H$^+$(1–0) is 6 × 2 arcmin^2. The reference position was taken at (−1500, 0) arcsec. In a further analysis, the OTF maps have been gridded with different steps ranging from 4 to 20 arcsec. Pointing and focus were checked on nearby strong continuum sources and Mars.

The 1.2-mm continuum observations were carried out in the autumn of 2010 during a pool session with the MAMBO2 bolometer array in the OTF mode. The antenna HPBW for these observations is about 11 arcsec. The data have been reduced by the MOPSIC package with skynoise filtering. The mean rms noise level calculated from the analysis of beam-sampled regions without noticeable emission is ∼10 mJy beam^{-1}.

2.2 OSO-20 observations

Observations with the 20-m telescope of the Onsala Space Observatory (OSO) were carried out in 2011 February. Maps of HCN(1–0) and HCO$^+$(1–0) have been obtained. Distinct positions have been observed in the H^{13}CN(1–0), H^{13}CO$^+$(1–0), C^{34}S(2–1) and CH$_3$OH(2–1) lines. We used a superconductor–insulator–superconductor (SIS) receiver in the frequency-switching mode with an autocorrelation spectrometer as a backend with 20 MHz and 25 kHz bandwidth and spectral resolution, respectively. The HCN and HCO$^+$ maps cover approximately 4 × 3 arcmin^2 around the central position, skipping the eastern–northern and southern–western corners of this rectangular region where lines are relatively weak. Mapping has been done with 20-arcsec grid spacing (Nyquist sampled maps). Pointing was checked periodically by observations of the R Cas SiO maser and is usually better than 5 arcsec. System temperatures were ∼300–500 K for HCN(1–0), ∼400–700 K for HCO$^+$(1–0) and ∼200–300 K for other molecular-line observations.

2.3 Effelsberg-100 observations

The NH_3 (1,1) and (2,2) observations with the Effelsberg-100 telescope were carried out in 2012 April. Both transitions were observed simultaneously using a receiver with a cooled high-electron mobility transistor (HEMT) amplifier. The extended bandwidth fast Fourier transform spectrometer (XFFTS) with a total bandwidth of 100 MHz and 3.05 kHz of spectral resolution was used. Mapping was done in the raster mode with a grid spacing of 20 arcsec (Nyquist sampling) in the frequency-switching mode. The region of observations was divided into two neighbouring subregions with sizes 140×160 and $100 \times 280 \, arcsec^2$ to the east and west of the central position, respectively. Pointing and focus have been checked periodically on both strong and nearby continuum sources. Pointing accuracy is $\lesssim 8$ arcsec. In order to convert the observed intensities into main beam temperatures, we took into account the opacity and gain-elevation corrections (A. Kraus, private communication). The primary calibration source NGC 7027 was used. The flux density was taken from Ott et al. (1994).

2.4 GMRT observations

The radio continuum observations at 1280 and 610 MHz were performed with the GMRT array on 2011 November 15 and 18. The GMRT consists of 30 antennas, each having a diameter of 45 m, which are located in a Y-shaped hybrid configuration. A central region of about 1 km^2 consists of 12 randomly distributed antennas. The rest are located along three radial arms up to ~ 14 km long (more technical details can be found in Swarup et al. 1991). The primary GMRT beams at 1280 and 610 MHz are 24 and 43 arcmin, respectively. At both frequencies, 3C286 and 3C48 were used as flux calibrators, and 1822-096 was used as phase calibrator. The data analysis was done with the AIPS package, including flagging corrupted data, calibration, Fourier inversion and cleaning. The resulting images have synthesized beams at 1280 and 610 MHz of 2.60×2.25 and $5.24 \times 4.79 \, arcsec^2$, respectively. The resulting rms are 0.16 and 0.75 mJy $beam^{-1}$ at 1280 and 610 MHz, respectively.

A comparison with the coordinates of the 3.6-cm VLA sources observed towards the W40 central region by Rodríguez et al. (2010) reveals systematic shifts of ~ 1.5 and ~ 4.5 arcsec between the VLA and the associated sources at 1280 and 610 MHz, respectively. The reasons for these shifts are unclear but probably are related to phase calibration at the GMRT. We have applied corresponding positional corrections to the GMRT maps to compensate for the shifts.

3 RESULTS AND DATA ANALYSIS

3.1 1.2-mm continuum data

The dust continuum emission map of the W40 region at 1.2 mm is shown in Fig. 1. The map reveals a ring-like structure consisting of dust clumps. This structure was previously detected by Maury
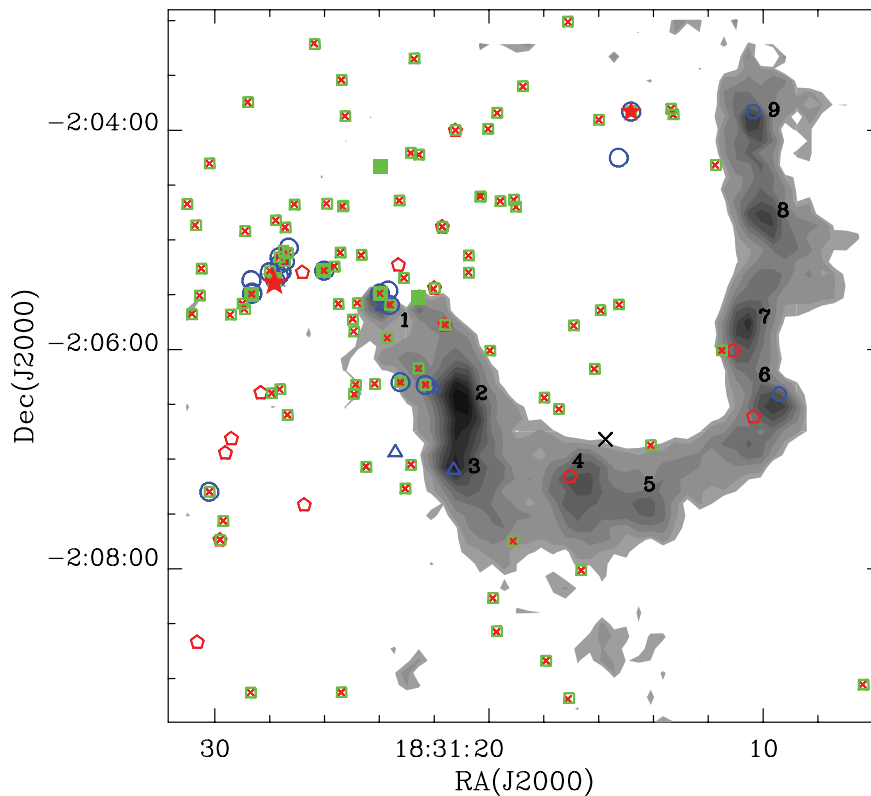
Figure 1. The W40 molecular cloud in the 1.2-mm dust continuum (grey-scale). Intensity contours range from 30 mJy $beam^{-1}$ (3σ) to 210 mJy $beam^{-1}$ with 10 mJy $beam^{-1}$ steps plus the 20 mJy $beam^{-1}$ contour in addition. The peak flux is 219.5 mJy $beam^{-1}$. The dust clumps for which we have derived physical parameters are marked by numbers. We show the compact VLA 3.6-cm sources from Rodríguez et al. (2010) (big blue circles), the NIR sources from Shuping et al. (2012) (filled green squares) and the 2MASS sources (empty green squares) coinciding with X-ray sources (Kuhn et al. 2010) (red crosses). The Class 0 and Class I sources from Maury et al. (2011) are shown as small blue circles and triangles, respectively. The Class I sources from Mallick et al. (2013) are shown as red pentagons. The peak ^{13}CO position (Zhu et al. 2006) is indicated as a black cross. The main driving source of the H II region (IRS 1A South) and the distinct IRS 5 source (Shuping et al. 2012) are marked by bigger and smaller red stars, respectively. Colour figures are available in the online version.

Table 2. Parameters of 1.2-mm continuum clumps.

Object	$\Delta\alpha$ (arcsec)	$\Delta\delta$ (arcsec)	Aspect ratio	$\Delta\Theta$ (arcsec)	d (pc)	F_{total} (mJy)	Associated sources
Clump 1	124.2(0.3)	72.7(0.2)	1.8(0.5)	9.6(1.2)	0.023(0.003)	188(7)	Class I[b]
Clump 2	79.3(0.2)	19.8(0.5)	2.0(0.1)	26.3(0.8)	0.064(0.002)	2910(21)[a]	Class I[b]
Clump 3	80.4(0.3)	−12.6(0.7)	1.4(0.2)	24.9(1.5)	0.060(0.004)		Class I[b]
Clump 4	12.1(0.3)	−29.7(0.6)	1.2(0.1)	45.1(2.0)	0.109(0.005)	1310(15)	Class I[c]
Clump 5	−20.1(0.5)	−36.4(0.4)	1.3(0.2)	30.7(1.8)	0.074(0.004)	519(10)	
Clump 6	−90.0(0.3)	18.5(0.4)	1.3(0.2)	24.2(1.8)	0.059(0.003)	737(11)	Class 0[b]
							Class I (?)[c]
Clump 7	−77.0(0.2)	62.5(0.4)	2.0(0.3)	22.7(1.4)	0.055(0.003)	527(8)	Class I (?)[c]
Clump 8	−88.0(0.3)	121.6(0.4)	1.9(0.2)	27.9(1.3)	0.068(0.003)	792(11)	
Clump 9	−80.8(0.4)	173.2(0.4)		5.8(2.1)	0.014(0.005)	570(9)	Class 0[b]

[a]Total flux for clumps 2 and 3.
[b]Maury et al. (2011).
[c]Mallick et al. (2013).

et al. (2011) in their 1.2-mm continuum study of the Aquila Rift complex. The 3.6-cm VLA sources (Rodríguez et al. 2010) and NIR sources (Shuping et al. 2012) are also shown in Fig. 1. Most of the NIR sources coincide with those detected earlier by Smith et al. (1985), being the members of the central cluster. Using the NIR spectroscopic data, Shuping et al. (2012) derived the spectral types of the sources and considered the IRS 1A South source (O9.5 type) to be the dominant source of LyC photons needed to power of the H II region (as opposed to IRS 2A as originally suggested by Smith et al. 1985). One of the NIR sources, IRS 5, of the B1 V spectral type (Shuping et al. 2012; Mallick et al. 2013) probably does not belong to the cluster. The IRS 5 source has a counterpart on the VLA maps (Rodríguez et al. 2010). Multiple NIR (Rodríguez et al. 2010), 2MASS, MSX mid-infrared sources, far-infrared sources (detected by *Herschel*; Bontemps et al. 2010) and *Chandra* X-ray sources (Kuhn et al. 2010) have also been detected in the region. The 2MASS and X-ray sources with position differences ≤1 arcsec, which could be tracers of young stellar objects (YSOs) embedded in the cloud, are also shown in Fig. 1. Most of these sources are located outside the ring in the east–north part of the map, but some of them can be associated with the eastern branch of the ring.

We deconvolved the dust map into nine individual clumps using our two-dimensional (2D) Gaussian fitting program (Pirogov et al. 2003). The clumps are marked by numbers (Fig. 1). Clumps 1 and 9 have dimensions lower than the antenna HPBW. The parameters of individual clumps are given in Table 2. It includes the relative offsets of the clump centres with respect to the central position, the aspect ratios, the deconvolved angular and linear sizes, estimated as the geometric mean of the extents of elliptical Gaussians (Columns 2–6). For clump 9, the results of the 2D circular Gaussian fit are given. Total fluxes of the clumps are given in Column 7. For clumps 2 and 3, which are closely located intensity enhancements over the local plateau approximately elongated in the north–south direction in the eastern branch of the ring, the total flux is given. Most strong 1.2-mm continuum emission comes from the eastern clumps, which are closer to the cluster sources. The IRS 2A and VLA 5–7 sources are associated with clump 1. The VLA 3 source is located near clump 2. The other clumps have no associated IR or radio sources.

Maury et al. (2011) have found, in total, 36 mm-continuum sources associated with the W40 region, 11 of which are located within the region observed by us. Three more sources from their survey are located outside our field of view to the north of IRS 5, but probably belong to the ring. Using the mm-continuum and *Herschel* data, they derived several physical parameters of the sources.

In further analysis, we have used their estimates of the dust temperature for the clumps, which are associated with their continuum sources. Several Class I sources from Mallick et al. (2013) are also located within the observed region. The last column of Table 2 gives the associations with the Class I and Class 0 sources found by Maury et al. (2011) and Mallick et al. (2013). The western dust clumps 6 and 9 are associated with Class 0 sources while the eastern clumps 2 and 3 can be associated with Class I sources (Maury et al. 2011). The Class I sources from Mallick et al. (2013) are located near the dust clumps 6 and 7 but are shifted from their centres. Their association with clumps is questionable.

3.2 Molecular-line data

The molecular-line maps of the W40 cloud show different morphologies, implying that there is a complicated structure of the region. Among the observed molecular lines, no one line appears to trace all the dust clumps of the ring. Some species show correlations with distinct dust clumps but some of them do not correlate with the dust continuum. Molecular emission is also found in the area with no prominent dust emission, implying that dense gas and dust do not follow each other.

3.2.1 Molecular-line maps

Molecular integrated intensity maps overlaid on the dust continuum image are shown in Fig. 2. Only the eastern part of the region has been mapped in $C^{34}S(2–1)$; in the other parts, $C^{34}S(2–1)$ observations have been done towards distinct positions. The CS lines are strong towards the eastern branch of the ring while the $N_2H^+(1–0)$ and $NH_3(1,1)$ lines are strong towards the western branch. The CS(5–4) map correlates with the eastern branch. The CS(2–1) map follows the dust ring in shape but is more extended. The HCN(1–0) and $HCO^+(1–0)$ maps cover an extended part of the region ($\sim 3 \times 2.5$ arcmin^2) and show practically no correlation with dust. The $H^{13}CO^+(1–0)$, $H^{13}CN(1–0)$ and $CH_3OH(2–1)$ lines are observed towards distinct positions. The $CH_3CCH(5–4)$ emission has not been detected in the region at the 3σ level of 0.06 K.

The $N_2H^+(1–0)$, $NH_3(1,1)$, CS(5–4) and $C^{34}S(2–1)$ maps are deconvolved into clumps in a similar way to the dust clumps (Section 3.1). We have also detected the CS clump, which lies to the south of the dust ring and is not associated with it (Fig. 2). Weak dust emission can be associated with this clump. No attempts have
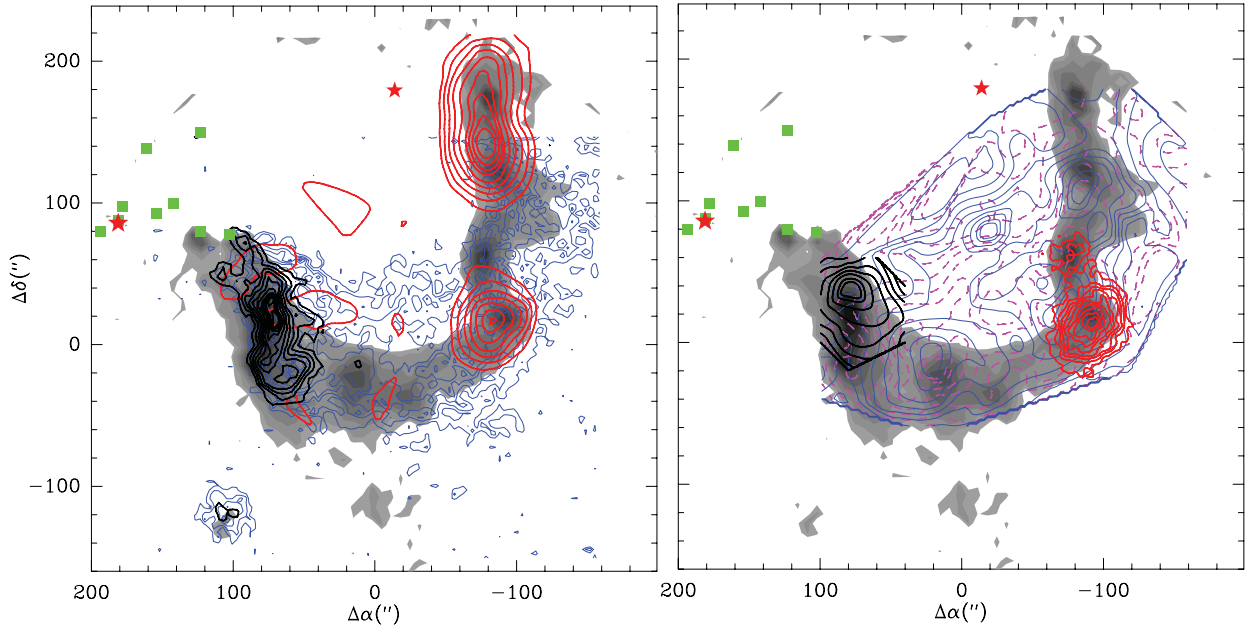
Figure 2. Molecular-line integrated intensity maps overlaid on 1.2-mm dust continuum emission (grey-scale). Left panel: CS(2–1) (blue contours), NH$_3$(1,1) (red contours), CS(5–4) (black contours). Right panel: HCN(1–0) (crimson dashed contours), HCO$^+$(1–0) (blue contours), N$_2$H$^+$(1–0) (red contours) and C^{34}S(2–1) (black contours). Intensity contours range from 20 to 90 per cent with steps of 10 per cent of the peak values plus the contour of 95 per cent. The peak integrated intensities (in K km s^{-1}) are 14.5 for CS(2–1), 36.5 for CS(5–4), 16.1 for NH$_3$(1,1), 15.6 for HCN(1–0), 10.9 for HCO$^+$(1–0), 22.7 for N$_2$H$^+$(1–0) and 2.2 for C^{34}S(2–1). Coordinates are the offsets with respect to the position of the ^{13}CO peak (Zhu et al. 2006). The NIR sources are marked by squares, the main driving source of the H ii region (IRS 1A South) is marked by a bigger red star and the IRS 5 source is marked by a smaller red star.

Table 3. Parameters of molecular clumps.

Object	$\Delta\alpha$ (arcsec)	$\Delta\delta$ (arcsec)	Aspect ratio	$\Delta\Theta$ (arcsec)	d (pc)	Associations with dust clumps
N$_2$H$^+$ clump	−90.1(0.2)	12.8(0.2)	1.8(0.1)	29.7(0.5)	0.072(0.001)	Clump 6
Ammonia clump 1	−82.4(1.1)	17.3(1.3)	2.2(0.9)	27.6(5.4)	0.067(0.013)	Clump 6
Ammonia clump 2	−77.9(0.8)	157.0(1.8)	4.7(1.3)	42.7(6.1)	0.104(0.015)	Clumps 8 and 9
CS(5–4) clump 1[a]	72.6(0.2)	18.5(0.7)	3.0(0.2)	30.9(0.8)	0.075(0.002)	Clump 2
CS(5–4) clump 2[b]	54.0(0.4)	−15.4(0.3)	1.7(0.2)	15.0(0.8)	0.036(0.002)	Clump 3 (?)
C^{34}S clump	71.3(2.8)	26.2(2.7)	1.5(0.5)	49.4(8.0)	0.12(0.02)	Clump 2
Southern CS clump	105.5(0.4)	−118.4(0.4)	1.3(0.2)	19.6(1.3)	0.048(0.003)	

[a]Integrated in the 6–9 km s^{-1} velocity range.
[b]Integrated in the 3–6 km s^{-1} velocity range.

been made to deconvolve the CS(2–1) clumps towards the eastern branch of the ring where the line profiles are multicomponent. Towards the other parts of the cloud, the CS(2–1) lines do not trace distinct clumps. The CS(5–4) clumps 1 and 2 are deconvolved from the intensity maps integrated in different velocity ranges. The derived parameters of molecular clumps are given in Table 3. In the last column, the associations with dust clumps are given. The centres and sizes of the N$_2$H$^+$ clump, the ammonia clump 1 and the dust clump 6 are close to each other. The ammonia clump 2 extends over both dust clumps 8 and 9 with the centre located between these dust clumps. Probably, the spatial resolution of the ammonia observations was not sufficient to resolve these closely located clumps. The area containing dust clumps 8 and 9 has not been observed in N$_2$H$^+$(1–0). The CS(5–4) clump 1 and the C^{34}S clump are associated with the dust clump 2.

3.2.2 Analysis of molecular spectra

After removing baselines from the data (low-order polynomials), line parameters have been obtained from Gaussian fitting. Table 4

includes integrated intensities and parameters of Gaussian fits (main beam temperature, velocity and linewidth) with corresponding 1σ errors towards selected positions. The positions are close to the CS, N$_2$H$^+$ or NH$_3$ (1,1) local integrated intensity peaks and corresponding clump centres. We also include the central position and positions to the north and to the south with respect to it (0, ±40) arcsec. For the purpose of comparison with the Onsala and Effelsberg data, the IRAM data have been averaged over areas with a 20-arcsec radius around given positions. The CS spectra towards the position of the southern CS clump observed only at IRAM are averaged for the area with a radius of 10 arcsec. No fitting has been done for the CS(2–1) lines towards the (80,40) and (80, 0) arcsec positions, because the profiles are multicomponent.

The N$_2$H$^+$(1–0) and NH$_3$ spectra observed towards the western part of the region show multiple and partly overlapping hyperfine components. These spectra are fitted with a function consisting of 7, 18 and 24 components for N$_2$H$^+$(1–0), NH$_3$ (1,1) and NH$_3$(2,2), respectively. Excitation temperatures are assumed to be the same within each group of overlapping components but can differ for different groups (three and five for N$_2$H$^+$ and NH$_3$, respectively).

Table 4. Molecular-line parameters towards selected positions.

Offsets (arcsec, arcsec)	Line	I (K km s^{-1})	T_{MB} (K)	V_{LSR} (km s^{-1})	ΔV (km s^{-1})	τ
(120, 60)	CS(2–1)	0.5(0.1)	0.26(0.03)	5.7(0.1)	1.8(0.2)	
		1.9(0.1)	0.67(0.04)	8.92(0.03)	1.2(0.1)	
	CS(5–4)	3.0(0.1)	1.4(0.1)	8.30(0.04)	2.0(0.1)	
	N$_2$H$^+$(1–0)		<0.15			
	NH$_3$(1,1)		<1.2			
(80, 40)	CS(2–1)	8.1(0.1)				
	CS(5–4)	15.1(0.2)	5.5(0.1)	7.37(0.02)	2.62(0.04)	
	C^{34}S(2–1)	1.9(0.1)	0.74(0.03)	7.07(0.05)	2.59(0.12)	
	N$_2$H$^+$(1–0)	0.7(0.1)	0.19(0.03)	6.97(0.06)	0.7(0.1)	
	NH$_3$(1,1)	1.5(0.2)	0.39(0.04)	6.4(0.1)	1.8(0.2)	
	HCN(1–0)	7.0(0.5)	1.9(0.1)	5.0(0.1)	1.8(0.1)	
	HCO$^+$(1–0)	2.8(0.4)	2.0(0.2)	4.5(0.1)	1.6(0.2)	
	H^{13}CN(1–0)	0.9(0.1)	0.5(0.1)	7.1(0.1)	1.4(0.3)	
(80, 0)	CS(2–1)	5.5(0.1)				
	CS(5–4)	16.2(0.1)	8.0(0.1)	7.83(0.01)	1.71(0.03)	
	C^{34}S(2–1)	1.4(0.1)	0.56(0.03)	7.68(0.05)	2.0(0.1)	
	N$_2$H$^+$(1–0)	1.3(0.1)	0.26(0.03)	8.03(0.04)	1.0(0.1)	
	NH$_3$(1,1)	1.3(0.3)	0.4(0.1)	8.1(0.1)	1.4(0.3)	
	HCN(1–0)	4.6(0.5)	1.7(0.2)	4.7(0.1)	1.7(0.2)	
	HCO$^+$(1–0)	4.3(0.4)	2.1(0.2)	4.5(0.1)	2.0(0.2)	
	H^{13}CN(1–0)	0.7(0.1)	0.27(0.02)	7.7(0.1)	2.0(0.2)	
	H^{13}CO$^+$(1–0)	0.26(0.05)	0.22(0.04)	7.4(0.1)	1.1(0.2)	
	CH$_3$OH(2–1)	0.27(0.04)	0.41(0.05)	7.98(0.04)	0.7(0.1)	
(−100, 20)	CS(2–1)	6.26(0.04)	4.40(0.04)	4.97(0.01)	1.37(0.01)	
	CS(5–4)	1.4(0.1)	1.04(0.06)	4.95(0.03)	1.3(0.1)	
	N$_2$H$^+$(1–0)	12.4(0.1)	8.5(0.3)[a]	4.663(0.003)	0.58(0.01)	4.6(0.6)
	NH$_3$(1,1)	10.5(0.2)	8.7(0.6)[a]	4.625(0.005)	0.52(0.02)	3.5(0.6)
	HCN(1–0)	8.7(0.5)	3.4(0.2)	4.82(0.04)	1.6(0.1)	
	HCO$^+$(1–0)	6.3(0.5)	4.4(0.2)	4.66(0.04)	1.4(0.1)	
	H^{13}CO$^+$(1–0)	1.0(0.1)	1.3(0.1)	4.63(0.02)	0.67(0.04)	
(−80, 140)	CS(2–1)	3.0(0.1)	3.7(0.6)	5.38(0.01)	0.74(0.01)	
	CS(5–4)		<0.5			
	NH$_3$(1,1)	16.0(0.1)	9.2(0.1)[a]	5.384(0.001)	0.387(0.004)	8.5(0.4)
(100, −120)	CS(2–1)	5.6(0.1)	3.4(0.1)	2.04(0.01)	1.54(0.03)	
	CS(5–4)	5.5(0.4)	3.2(0.2)	2.04(0.05)	1.5(0.1)	
(0, 0)	CS(2–1)	7.64(0.03)	4.77(0.02)	4.91(0.01)	1.50(0.01)	
	CS(5–4)	3.2(0.1)	1.5(0.1)[b]	5.07(0.03)	1.2(0.1)	
	C^{34}S(2–1)	0.7(0.1)	0.42(0.04)	4.92(0.05)	1.2(0.1)	
	N$_2$H$^+$(1–0)	0.4(0.1)	0.06(0.01)	5.0(0.1)	1.7(0.1)	
	NH$_3$(1,1)	3.4(0.4)	0.46(0.05)	5.4(0.1)	2.9(0.4)	
	HCN(1–0)	12.6(0.3)	4.4(0.1)	4.98(0.02)	1.7(0.1)	
	HCO$^+$(1–0)	9.2(0.5)	4.7(0.2)	4.62(0.03)	1.7(0.1)	
	H^{13}CN(1–0)		<0.3			
	H^{13}CO$^+$(1–0)	0.39(0.04)	0.27(0.03)	4.9(0.1)	1.4(0.2)	
(0, 40)	CS(2–1)	3.52(0.04)	2.43(0.03)	5.03(0.01)	1.39(0.02)	
	CS(5–4)	0.8(0.1)	0.45(0.04)	5.3(0.1)	1.8(0.2)	
	N$_2$H$^+$(1–0)		<0.1			
	NH$_3$(1,1)	1.6(0.3)	0.23(0.05)	5.0(0.2)	2.5(0.6)	
	HCN(1–0)	12.8(0.4)	4.5(0.1)	5.04(0.02)	1.6(0.1)	
	HCO$^+$(1–0)	9.2(0.5)	4.7(0.2)	4.62(0.03)	1.7(0.1)	
(0, −40)	CS(2–1)	6.35(0.04)	3.25(0.03)	4.96(0.01)	1.89(0.02)	
	CS(5–4)	2.6(0.1)	1.41(0.03)	5.44(0.02)	1.7(0.1)	
	N$_2$H$^+$(1–0)		<0.1			
	NH$_3$(1,1)	3.1(0.3)	0.40(0.05)	5.3(0.2)	2.8(0.4)	
	HCN(1–0)	10.2(0.4)	3.1(0.1)	5.03(0.03)	1.8(0.1)	
	HCO$^+$(1–0)	6.1(0.4)	3.2(0.2)	4.64(0.05)	1.8(0.1)	

[a]The T_{EX} value of the main group of hyperfine components.
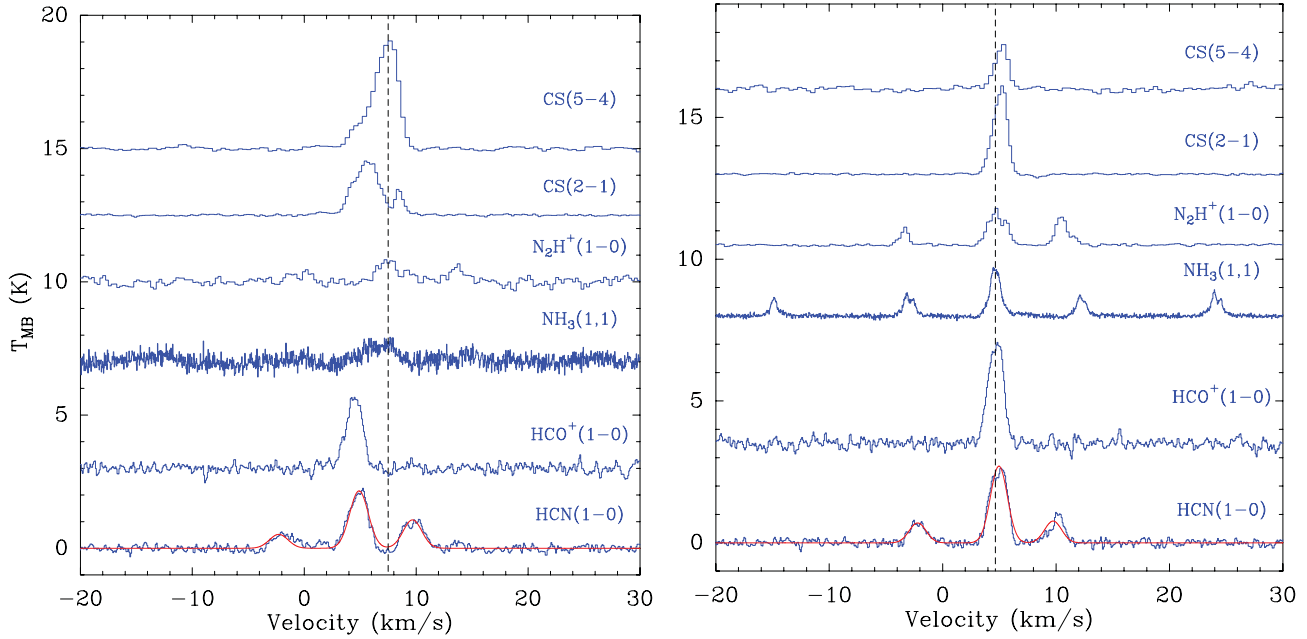[b]The spectrum possesses two overlapping components, the second one of lower intensity at ∼6.7 km s^{-1}.

Figure 3. Molecular-line spectra averaged over (left panel) the eastern ($\Delta\alpha = 100$ to 40 arcsec, $\Delta\delta = -50$ to 60 arcsec) and (right panel) the western ($\Delta\alpha = -50$ to -140 arcsec, $\Delta\delta = -50$ to 60 arcsec) parts of the region observed. Dashed vertical lines correspond to 7.5 km s^{-1} (left panel) and to 4.65 km s^{-1} (right panel). The results of the HCN(1–0) fitting by a Gaussian triplet of the same width are also shown by the smooth curve.

The method was used previously for fitting the N$_2$H$^+$(1–0) spectra (Pirogov et al. 2003). The fitting parameters are the number of excitation temperatures equal to the number of groups of hyperfine components, the velocity of the central component, the linewidth and the total optical depth. For the $(-100, 20)$ and $(-80, 140)$ arcsec positions (Table 4), the N$_2$H$^+$(1–0) and NH$_3$(1,1) excitation temperatures of the main (central) group of hyperfine components are given instead of the main beam temperatures.

The HCN(1–0) spectra consist of three hyperfine components and have been fitted by three Gaussians of the same width. The $F = 1 - 1$ HCN(1–0) hyperfine component (the red component) in the central and western parts of the observed region is systematically shifted with respect to the expected position. The profiles of individual hyperfine components often deviate from the Gaussian. Probably, different HCN(1–0) hyperfine components trace gas with slightly different velocities. Because the signal-to-noise ratios are not high, fitting of the HCN(1–0) spectra by more than one closely located Gaussian triplet is often ambiguous. Therefore, the results of fitting by a single triplet are given in Table 4. The main beam temperature corresponds to the central hyperfine component $F = 2 - 1$. We do not use these results in further analysis.

Towards the eastern part of the region, the observed lines can be roughly divided into two velocity ranges. The HCN(1–0) and HCO$^+$(1–0) lines are observed at ~ 4.5–5 km s^{-1} and other lines are observed at ~ 7–8 km s^{-1}. The averaged CS(5–4), CS(2–1), N$_2$H$^+$(1–0), NH$_3$(1,1), HCO$^+$(1–0) and HCN(1–0) spectra for the eastern and western areas are shown in the left and right panels of Fig. 3, respectively. The HCN(1–0) fitting results are also shown in both panels. The CS(2–1) profiles in the eastern area are self-reversed. Both CS lines in the eastern area have extended blue wings probably because of emission at ~ 4.5–5 km s^{-1}. Weak H^{13}CN(1–0) and H^{13}CO$^+$(1–0) emission is detected towards distinct eastern positions at ~ 7.3–7.5 km s^{-1} (Table 4). No HCN(1–0) or HCO$^+$(1–0) emission has been detected at these velocities. There is a hint of weak absorption in the HCN(1–0) spectra at ~ 7.5 km s^{-1}

Table 5. Physical parameters derived from 1.2-mm continuum data.

Object	T_d (K)	$M(\mathrm{M}_\odot)$	N_{H_2} (cm^{-2})	$\bar{n}$ (cm^{-3})
Clump 1	36[a]	0.4	2.5×10^{22}	3.1×10^5
Clump 2	27[a]	8.1[c]	6.2×10^{22}	1.8×10^5
Clump 3	28[a]		5.2×10^{22}	6.6×10^5
Clump 4	20[b]	5.6	5.2×10^{22}	1.0×10^5
Clump 5	20[b]	2.2	4.3×10^{22}	1.4×10^5
Clump 6	18[a]	3.6	7.0×10^{22}	2.9×10^5
Clump 7	20[b]	2.2	7.3×10^{22}	2.8×10^5
Clump 8	13[a]	6.2	1.1×10^{23}	3.6×10^5
Clump 9	23[a]	2.0	6.2×10^{22}	1.4×10^6

[a]Dust temperatures taken from Maury et al. (2011).
[b]Assumed dust temperature.
[c]Total mass for clumps 2 and 3.

in the eastern area (Fig. 3, left panel). We briefly discuss this phenomenon in Section 7.4.

The linewidths in different parts of the cloud lie in the range ~ 1–2 km s^{-1} (Table 4), much higher than the thermal widths (the ammonia kinetic temperatures and dust temperatures are given in Tables 5 and 6, respectively). Enhanced linewidths of weak ammonia lines towards the central and eastern positions are probably a result of the systematic uncertainties of the fits for the spectra with low signal-to-noise ratios. The broadening of the CS(5–4) and C^{34}S(2–1) lines towards (80, 40) arcsec can be connected with enhanced dynamical activity and the presence of systematic motions (Section 5.3). Towards the $(-100, 20)$ arcsec position close to the centre of the dust clump 6, the N$_2$H$^+$, NH$_3$ and H^{13}CO$^+$ lines are more narrow (0.5–0.7 km s^{-1}) than the CS, HCN and HCO$^+$ lines (1.3–1.6 km s^{-1}). This could be a result of both optical depth effects and the fact that the lines trace different gas components on the line of sight with different extents of turbulence (e.g. the quiescent region within the clump and the surrounding gas with a higher extent of

Table 6. Ammonia kinetic temperatures and LTE column densities.

$(\Delta\alpha, \Delta\delta)$ (arcsec, arcsec)	T_{KIN} (K)	$N(NH_3)$ (cm^{-2})	$N(N_2H^+)$ (cm^{-2})	$N(H^{13}CN)$ (cm^{-2})	$N(H^{13}CO^+)$ (cm^{-2})	$N(C^{34}S)$ (cm^{-2})	Associated objects
(80, 40)		6.0×10^{13}	7.3×10^{11}	1.4×10^{12}		2.1×10^{13}	Dust clump 2
(80, 0)		5.2×10^{13}	1.3×10^{12}	1.1×10^{12}	2.4×10^{11}	1.1×10^{13}	Dust clump 3
(0, 0)		8.4×10^{13}	4.2×10^{11}		3.6×10^{11}	2.9×10^{12}	^{13}CO peak
(0, −40)		8.1×10^{13}					
(0, 40)		5.0×10^{13}					
(−100, 20)	20.7(2.5)	2.5×10^{14}	1.5×10^{13}		8.3×10^{11}		Dust clump 6
(−80, 140)	15.9(0.4)	5.7×10^{14}					Ammonia clump 2

turbulence, respectively). Most narrow lines are detected towards the (−80, 140) arcsec position (ammonia clump 2), implying the lowest extent of turbulence.

3.3 Comparison with CO data

The W40 molecular cloud has been mapped previously in the CO isotopic lines by different authors (Zeilik & Lada 1978; Crutcher & Chu 1982; Vallée et al. 1992; Zhu et al. 2006). The ^{13}CO(3–2) map from Zhu et al. (2006) overlaid on our dust continuum map is shown in Fig. 4. They also found an implication for the weak CO outflow in the centre of the map. No corresponding dust or molecular emission peaks are found near this position in our observations. The shape of the ^{13}CO(3–2) map in the western part is curved to the north, correlating in general with the shape of the dust ring. Yet, the spatial resolution (∼80 arcsec) is too low to resolve the structure of the emission region in detail. The CO emission is also detected towards the centre of the H II region and to the east from the centre. The CO and ^{13}CO spectra consist of the main component at ∼4.5–5 km s^{-1} and weak satellites in emission and in absorption at higher velocities. Near the centre of the H II region, an additional component at ∼9–10 km s^{-1} with an intensity of the order of the
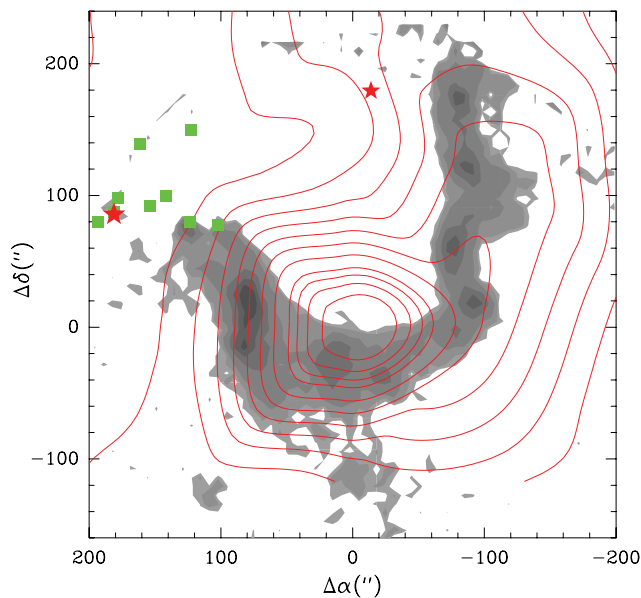

Figure 4. The ^{13}CO(3–2) integrated intensity map observed by Zhu et al. (2006) (red contours) is overlaid on 1.2-mm dust continuum emission (grey-scale). Intensity contours range from 10 to 90 per cent with steps of 10 per cent of the peak value (39.5 K km s^{-1}) plus the contour of 95 per cent. The rest of the symbols are the same as in Fig. 2.

main component appears on the spectra. For three central positions of our region with no kinetic or dust temperature estimates, we have taken the CO(1–0) peak main beam temperatures as crude estimates of kinetic temperature in model calculations (Section 5.2).

4 PHYSICAL PARAMETERS DERIVED FROM MM-CONTINUUM DATA

Table 5 gives the physical parameters of the dust clumps. Dust temperatures (T_d) are taken from Maury et al. (2011) for the clumps associated with their sources. The eastern clumps, which are closer to the cluster sources, have higher dust temperatures compared to the southern and western clumps. For the remaining clumps, dust temperatures are set to 20 K. Dust masses are calculated as (e.g. Doty & Leung 1994)

$$M_d = \frac{F_{total} D^2}{k_{1.2} B_{1.2}(T_d)}, \qquad (1)$$

where D, $k_{1.2}$ and $B_{1.2}(T_d)$ are the source distance, the dust mass absorption coefficient and the Planck function at 1.2 mm, respectively. For circumstellar envelopes around Class I and Class 0 protostars, the mass absorption coefficient can be taken to be equal to 1 cm^2 g^{-1} (Motte, André & Neri 1998), the value at the 1.3-mm wavelength appropriate for cold dust grains covered with thick icy mantles (Ossenkopf & Henning 1994). We have used this value in our calculations. For pre-stellar dense clumps, Motte et al. (1998) adopted $k_{1.2} = 0.5$ cm^2 g^{-1}. If we take this value for the sourceless clumps 5 and 8, their masses, column densities and number densities will be two times higher. Gas masses are calculated as $M = R_m M_d$. A gas-to-dust mass ratio, R_m, is taken to be equal to 100. The uncertainties of masses (∼30–35 per cent) are calculated with the propagation of errors method using the uncertainties of fluxes, dust temperatures uncertainties (∼20 per cent, according to Maury et al. 2011) and distance (∼10 per cent according to Shuping et al. 2012).

Peak hydrogen column densities (N_{H_2}) have been calculated from peak flux-per-beam and dust temperature values (e.g. Motte et al. 1998)

$$N_{H_2} = \frac{F_{peak}}{\Omega m R_m^{-1} k_{1.2} B_{1.2}(T_d)}, \qquad (2)$$

where Ω is the beam solid angle and $m = 2.33$ amu is mean molecular mass. The N_{H_2} positions are located close to the positions of the clump centres (Table 2). The N_{H_2} values are given in column 4 of Table 5. The calculated uncertainties of the N_{H_2} values are ∼25–35 per cent. Besides, we have calculated the mean volume densities for the individual clump areas ($\bar{n}$) as the mean column density divided by the clump size (Table 2). These are given in the last column of Table 5.

5 PHYSICAL PARAMETERS DERIVED FROM MOLECULAR-LINE DATA

Molecular-line data are used to derive the physical parameters of the gas (kinetic temperatures, densities, column densities, abundances and virial masses) using either the local thermodynamic equilibrium (LTE) approximation or non-LTE modelling. For most positions, we assume that the dust coexists with the gas traced by molecular lines. For the positions with no kinetic or dust temperature estimates, we have used the CO(1–0) line peak temperatures as a measure of kinetic temperature. However, the CO line velocities usually differ slightly from the velocities of the other lines.

5.1 Kinetic temperatures and column densities derived from LTE analysis

We have derived the NH_3 column densities in the LTE approximation using the procedures from Harju, Walmsley & Wouterloot (1993). For the western positions where ammonia lines are strong, we used the (1,1) linewidth, total optical depth and excitation temperature as well as the integrated intensity of the optically thin (2,2) line in the calculations. Kinetic temperatures are calculated from rotational temperatures using an empirical relation from Tafalla et al. (2004). The $N(NH_3)$ and T_{KIN} values for the positions close to the centres of ammonia clumps are given in Table 6. The uncertainties of the kinetic temperatures are estimated by the propagation of errors method using the uncertainties of integrated intensities and uncertainties of fits. The uncertainties of column densities are ∼10–30 per cent. The kinetic temperature of the ammonia clump 1 is close to the dust temperature of the associated dust clump 6 (Table 5). The kinetic temperature of the ammonia clump 2 is higher than the dust temperature of the dust clump 8 and is lower than of the dust clump 9. A kinetic temperature map has been obtained for the ammonia clump 2. It shows no apparent spatial variations. The NH_3 column densities for the eastern and central positions are calculated from the (1,1) integrated intensities in the LTE and the optically thin approximation taking excitation temperature equal to 10 K. The $N(NH_3)$ uncertainties for these positions are connected mainly with unknown excitation temperature and can reach ∼60 per cent.

The $N_2H^+(1–0)$ line towards the (−100, 20) arcsec position is optically thick and has an excitation temperature close to the $NH_3(1,1)$ line (Table 4). The $H^{13}CO^+$ column density for this position is calculated with the same value of excitation temperature. The $H^{13}CN$, $H^{13}CO^+$ and N_2H^+ column densities towards the eastern and central positions are calculated in the LTE and optically thin approximation, taking $T_{EX} = 10$ K. The $N(C^{34}S)$ values are calculated for

three selected positions under the same assumptions. The $C^{34}S$ excitation temperature for the (80, 40) arcsec position is taken to be equal to 50 K, according to the results of non-LTE model calculations (Section 5.3). For the (80, 0) and (0, 0) arcsec positions, the $C^{34}S$ excitation temperatures are taken to be equal to 30 and 10 K, respectively. The calculated values are given in Table 6.

5.2 Physical parameters derived from non-LTE analysis

Knowing the kinetic temperature, molecular column density and peak molecular-line intensity and width, it is possible to derive the number density using the non-LTE (large velocity gradient or microturbulent) approach for the homogeneous isothermal model. If two different transitions of the same molecule are observed, as in the case of CS, it is possible to obtain the molecular column density and number density from the observed peak line intensities and widths.

We have used the RADEX non-LTE radiative transfer online code (Van der Tak et al. 2007) and have derived the number densities and CS column densities towards selected positions where the CS line profiles are close to Gaussian. Kinetic temperatures are taken close to the ammonia (Table 6) or dust temperatures (Table 5). For the (0, 0) and (0, ±40) arcsec positions, estimates of the kinetic temperatures are close the CO(1–0) main beam temperatures. In order to derive parameters towards one selected eastern position where the CS(2–1) line profile is non-Gaussian and self-absorbed, we performed model calculations in the framework of the inhomogeneous non-LTE model (Section 5.3).

Having calculated the number densities, we used RADEX to obtain the column densities of other species, assuming they coexist with CS. The results are given in Table 7. The derived column densities of the optically thin $H^{13}CO^+(1–0)$ and $N_2H^+(1–0)$ lines are practically the same as those derived from the LTE analysis (Table 6), confirming the validity of the LTE approximation. The upper limit on number density and the lower limit on the CS column density are derived for the (−80, 140) arcsec position, where only the upper limit on the CS(5–4) line temperature is measured. Towards the (120, 60) arcsec position (dust clump 1), the CS(2–1) spectrum consists of two peaks (Table 4), while the CS(5–4) profile is single-peaked. The CS(5–4) and CS(2–1) (red peak) velocities are 8.3 and 8.9 km s^{-1}, respectively. The physical parameters derived on the basis of these line parameters should be treated with caution. The derived number densities are higher than the mean densities of the associated dust clumps (Table 5).

Taking the N_2H^+ emission region size and the N_2H^+ linewidth, we have calculated the virial mass for the N_2H^+ clump (associated

Table 7. Parameters derived from the non-LTE modelling.

$(\Delta\alpha, \Delta\delta)$ (arcsec, arcsec)	T_{KIN} (K)	n (cm^{-3})	$N(CS)$ (cm^{-2})	$N(HCO^+)$ (cm^{-2})	Associated object
(120, 60)	36	3.2×10^6 [a]	6.3×10^{12} [a]		Dust clump 1
(80, 40)	40	1.5×10^6 [b]	1.7×10^{14}		Dust clump 2
(0, 0)	25	5.0×10^5	2.9×10^{13}	9.0×10^{12}	^{13}CO peak
(0, −40)	20	1.0×10^6	3.0×10^{13}	7.0×10^{12}	
(0, 40)	25	3.3×10^5	1.5×10^{13}	8.5×10^{12}	
(−100, 20)	20	5.1×10^5	3.0×10^{13}	6.8×10^{12}	Dust clump 6
(−80, 140)	16	$\lesssim 10^5$	$\gtrsim 1.5 \times 10^{13}$		Ammonia clump 2
(100, −120)	26	1.8×10^6	3.0×10^{13}		Southern CS clump

[a]Because of the difference between the CS(2–1) and (5–4) velocities, these estimates are questionable.
[b]The density for the core centre; the density in the envelope is 1.5×10^3 cm^{-3} (Section 5.3).

with the ammonia clump 1 and the dust clump 6), assuming that it is spherically symmetric with no external pressure and no magnetic field: $M_{VIR} = 105 \, \Delta V^2 \, (1.2 \, d)$. The coefficient 1.2 is used to convert the FWHM size to the size at the e^{-1} level to be compared with mass estimated from the 1.2-mm continuum data. The derived virial mass, $\sim 3 \, M_\odot$, is in general agreement with the mass derived from the continuum data (Table 5), taking into account possible uncertainties. Virial mass for the ammonia clump 2 ($\sim 1.9 \, M_\odot$) derived from the ammonia data is close to the mass of the dust clump 9.

5.3 Non-LTE modelling of CS spectra with the inhomogeneous model

Towards the eastern branch of the dust ring (the area that includes the dust clumps 2 and 3), the CS(5–4) lines are the most intensive and single-peaked, while the CS(2–1) profiles are asymmetric and self-absorbed. The CS line profiles towards (80, 40) arcsec (Fig. 5) are affected to a lesser extent by the emission at lower velocities, compared with other positions in this area. We have used these for the modelling.

The velocity of the absorption dip on the CS(2–1) profile is close to the peak of the $C^{34}(2-1)$ profile, which is probably optically thin (Fig. 5). This implies that the observed CS(2–1) profile asymmetry is connected with systematic motions on the line of sight. The type of asymmetry with the blue peak stronger than the red peak can be a result of the infall motions on the line of sight, as predicted by the inside-out model of low-mass star formation (Shu 1977; Evans 1999). The signatures of infall on line profiles are widely observed, in both low-mass and high-mass star forming regions (e.g. Lee, Myers & Tafalla 2001; Klaassen & Wilson 2007; Sohn et al. 2007; Wu et al. 2007). If the gas on the line of sight is contracting, a crude estimate of the infall velocity, V_{IN}, can be made with the two-layer model (Myers et al. 1996). We calculated a V_{IN} value for the CS(2–1) profile of $\sim 0.24 \, km \, s^{-1}$. The kinematic mass infall rate can be estimated as $dM/dt = 4\pi \, r_{in}^2 \, m \, n_0 \, V_{IN}$ (Myers et al. 1996; Klaassen & Wilson 2007), where r_{in} is the radius of the infall region, m is the mean molecular mass and n_0 is an ambient density. Taking $r_{in} \sim$

0.05 pc (20 arcsec at a distance of 500 pc) and $n_0 \sim 1.5 \times 10^3 \, cm^{-3}$ (the density of the envelope, see below), the crude estimate for the mass infall rate is $\sim 2.7 \times 10^{-6} \, M_\odot \, yr^{-1}$. This is much lower than the mass infall rates calculated for HMSF regions (e.g. Fuller, Williams & Sridharan 2005; Klaassen & Wilson 2007) or massive YSOs (Chen et al. 2010), and is more in accordance with the values for low-mass starless cores (Lee et al. 2001). Note that we used an arbitrary value of r_{in} in the calculations.

In order to obtain other physical parameters of molecular gas towards the (80, 40) arcsec position, we performed model calculations of CS line excitation and we fitted the model profiles to those observed. The microturbulent multilayer spherically symmetric model has been used. Layer widths are scaled logarithmically and the physical parameters are the functions of layer radius. In addition to the number of logarithmically scaled layers (core), an outer layer (envelope) with constant density is added in order to allow absorption of the CS(2–1) emission in the low-density gas. The method of calculations is similar to that described by Turner, Pirogov & Minh (1997) (see their appendix). In order to take into account the systematic velocity field, each layer is divided into the number of steps at which the projection of systematic velocity is calculated. Systematic velocity is set to zero in the central layer. Number density and systematic velocity fall down outwards, according to the power-law radial profiles. Kinetic temperature, turbulent velocity dispersion and CS abundance are set constant throughout the cloud. We have used the CS–H_2 collisional rates tabulated for given kinetic temperatures by Turner et al. (1992).

The results of the model calculations are shown in Fig. 5 as smooth curves overlaid on the observed line profiles. The model parameters are $T_{KIN} = 40 \, K$, $V_{IN} = 0.5(r/R_0)^{-0.1} \, km \, s^{-1}$, $R_{core}/R_0 = 33$ and $R_{env}/R_{core} = 40$, where R_0, R_{core} and R_{env} are the radii of the central layer, the core and the envelope, respectively. The total column densities are $N(CS) = 1.7 \times 10^{14} \, cm^{-2}$ and $N(C^{34}S) = 2 \times 10^{13} \, cm^{-2}$. The densities and turbulent velocity dispersions in the core and in the envelope are $n_{core}(r) = 1.5 \times 10^6(r/R_0)^{-2} \, cm^{-3}$, $n_{env} = 1.5 \times 10^3 \, cm^{-3}$, $V_{core} = 1.4 \, km \, s^{-1}$ and $V_{env} = 0.7 \, km \, s^{-1}$. The envelope effectively absorbs the CS(2–1) emission, producing a self-adsorption dip on the line profile, while the presence of infall motions makes the CS(2–1) profile asymmetric. The V_{IN} value at the boundary of the cloud is $\sim 0.25 \, km \, s^{-1}$ in accordance with the crude estimate of the two-layer model (Myers et al. 1996). Table 7 gives the total CS column density and number density in the centre of the core derived from the model.

The peak on the observed CS(5–4) profile is shifted by $\sim 0.2 \, km \, s^{-1}$ to higher velocities with respect to the peak of the $C^{34}S(2-1)$ profile and the self-absorption dip on the CS(2–1) profile. If this is connected with an absorption of the CS(5–4) blue wing in the foreground gas (which is probably seen on the $C^{34}S(2-1)$ profile), the observed CS(5–4) intensities could be underestimated and the central density in the core could be higher.

5.4 Molecular and electron abundances

Molecular abundances are given in Table 8. They are calculated as the ratios of molecular column densities (Tables 6 and 7) to the H_2 column densities, $N_{MOL}/N(H_2)$. The latter have been calculated using equation (2) for areas with a 20-arcsec radius around selected positions using the dust temperature or kinetic temperature estimates (Table 7). No abundance estimates have been made towards the (0, 40) arcsec position, where no noticeable dust continuum emission is detected and dense gas and dust apparently do

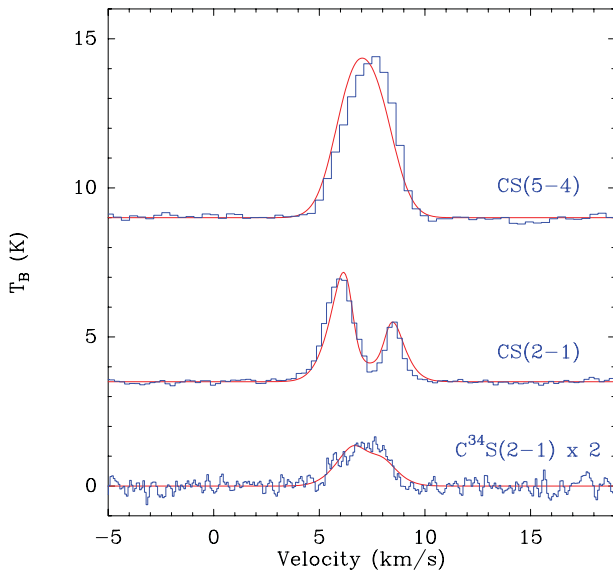**Figure 5.** The observed CS(5–4), CS(2–1) and $C^{34}S(2-1)$ line profiles towards the (80, 40) arcsec position. The results of model calculations in the framework of the inhomogeneous microturbulent model with systematic motions are shown as red smooth curves (see text for details).

Table 8. Molecular and electron abundances.

$(\Delta\alpha, \Delta\delta)$ (arcsec, arcsec)	$X(NH_3)$	$X(N_2H^+)$	$X(CS)$	$X(C^{34}S)$	$X(HCO^+)$	$X(H^{13}CO^+)$	$X(H^{13}CN)$	$X(e)$
(120, 60)			8.3×10^{-10}					
(80, 40)	2.5×10^{-9}	3.0×10^{-11}	7.1×10^{-9}	8.3×10^{-10}			5.8×10^{-11}	
(80, 0)	1.5×10^{-9}	3.8×10^{-11}		3.2×10^{-10}		7.1×10^{-12}	3.2×10^{-11}	
(0, −40)	2.6×10^{-9}		9.7×10^{-10}		2.3×10^{-10}			1.7×10^{-7}
(−100, 20)	9.3×10^{-9}	5.6×10^{-10}	1.1×10^{-9}		2.5×10^{-10}	3.1×10^{-11}		3.1×10^{-7}
(−80, 140)	1.5×10^{-8}		$>4 \times 10^{-10}$					
(100, −120)			8.3×10^{-9}					
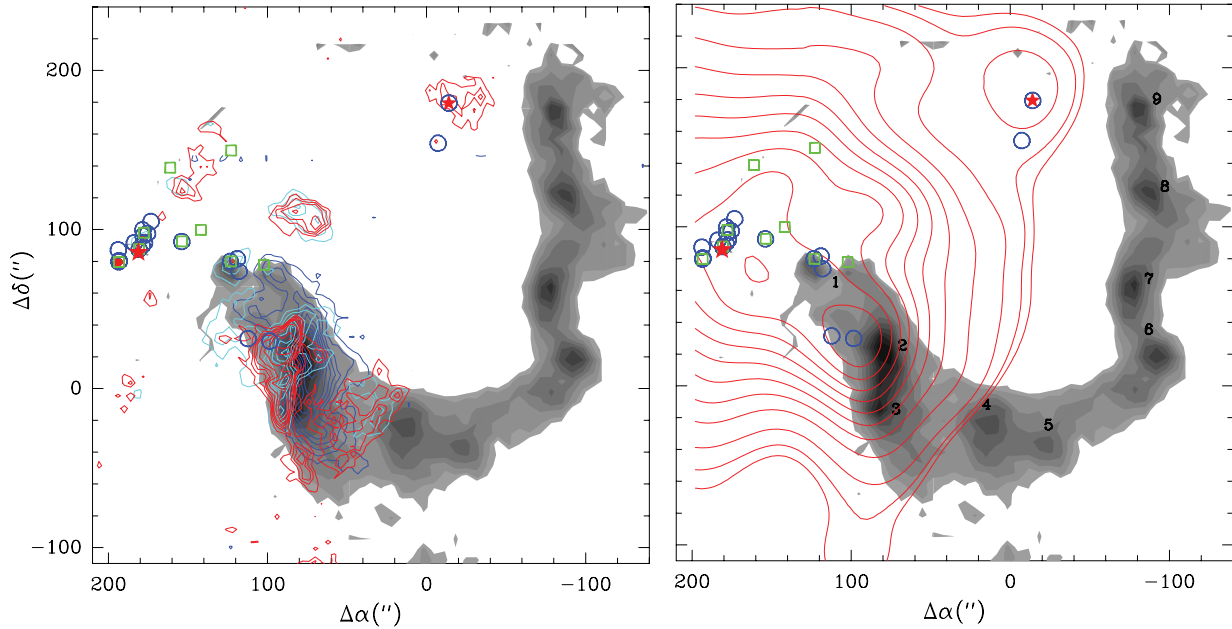
Figure 6. Left panel: the high-resolution 1280- and 610-MHz maps (spatial resolutions ∼2.4 and ∼5 arcsec, respectively) and the CS(5–4) integrated intensity map (red, cyan and blue contours, respectively). The 1280-MHz contours are 0.5, 0.7, 0.9, 1.1, 1.5, 2, 3, 4 and 5 mJy beam^{-1}. The 610-MHz contours range from 3 to 10 mJy beam^{-1} with steps of 1 mJy beam^{-1}. The CS(5–4) contours range from 10 to 90 per cent of the peak value (19.9 K km s^{-1}) with steps of 10 per cent. Right panel: the low-resolution 1280-MHz map (∼45 arcsec) at 3 and 5 per cent and from 10 to 90 per cent of the peak flux (449 mJy beam^{-1}) with steps of 10 per cent (Mallick et al. 2013). The dust clumps are marked by numbers on the right panel. The contour maps on both panels are overlaid on the dust continuum image (grey-scale). The rest of the symbols are the same as in Fig. 2.

not coexist there. We have not estimated abundances for the (0, 0) arcsec position where the coexistence of gas and dust is also questionable (Fig. 2).

Molecular abundances vary greatly throughout the cloud. The abundances of nitrogen-bearing molecules (NH$_3$ and N$_2$H$^+$) and of H^{13}CO$^+$ are enhanced towards western positions while the CS abundances are enhanced towards the eastern position (80, 40) arcsec (dust clump 2) and in the southern CS clump.

Using the HCO$^+$ abundance and number density, it is possible to estimate electron abundance, $X(e)$, using the relation that follows from equations of formation and destruction of the HCO$^+$ and H$_3^+$ ions in dense interstellar clouds (e.g. Zinchenko, Caselli & Pirogov 2009):

$$X(HCO^+) = \frac{\zeta/n}{\alpha(HCO^+)\,X(e) + k_g\,X_g}. \quad (3)$$

We have assumed that the cosmic ray ionization rate is equal to $\zeta = 3 \times 10^{-17}$ s^{-1}, while the HCO$^+$ dissociative recombination rate, $\alpha(HCO^+)$, is assumed to be equal to 7.5×10^{-7} s^{-1} cm^3 (Turner 1995). The HCO$^+$ recombination on to negatively charged dust grains (the term $k_g\,X_g$, where k_g and X_g are the rate coefficient and

the abundance of dust grains, respectively) is much lower compared with the cosmic ray ionization rate divided by the product of number density and HCO$^+$ abundance, and it can be neglected (Zinchenko et al. 2009). The calculated electron abundances are given in Table 8. They are among the highest values of $X(e)$ derived for both low-mass star-forming (Caselli et al. 1998) and HMSF (Zinchenko et al. 2009) regions. A brief discussion on the derived abundances is given in Section 7.4.

6 MORPHOLOGY OF THE IONIZED GAS

Mallick et al. (2013) have given low-resolution 1280- and 610-MHz images of the W40 H II region derived from our GMRT data. The H II region appears to be bounded to the west of the main ionizing source (IRS 1A South) by dense gas and dust. We used high-resolution GMRT maps to study in detail the interaction region between ionized and dense neutral gas and dust. The 1280- and 610-MHz maps and the CS(5–4) intensity map integrated in the 6–9 km s^{-1} velocity range are shown in Fig. 6 (left panel). The maps are overlaid on the dust continuum image.

We have detected an area of enhanced intensity close to the eastern branch of the dust ring. This area was observed previously at 1465 MHz by Vallée & MacLeod (1991). Our interferometric maps reveal the complex clumpy structure of the ionized gas in this area. The shapes of ionized, molecular and dust maps are similar, in general. Yet, the ionized gas region is slightly shifted (by several arcsec) to the east with respect to the dust and the CS(5–4) emission regions. The low-resolution image shows that ionized gas emission extends to the west of the cluster, up to the central position on our maps (^{13}CO peak) and includes a compact area around IRS 5 at the north-west (Fig. 6, right panel). There is another local emission subregion on the 1280-MHz low-resolution map close to the dust clump 2 (Fig. 6, right panel). This could also be a Strömgren sphere around a young massive star. The VLA 3 source with the 2MASS, X-ray counterparts is located in the centre of this subregion. There is a closely located Class I source (Fig. 1). We have calculated the fluxes of the enhanced intensity area ($\Delta \alpha = 120$ to 70 arcsec, $\Delta \delta = -40$ to 50 arcsec), which are $F(1280) = 502(1)$ and $F(610) = 555(2)$ mJy. The spectral index (~ -0.14) is close to the value expected for optically thin free–free emission.

7 DISCUSSION

7.1 Clumpy ring

The structure observed in the 1.2-mm continuum ring consists of regularly spaced clumps, which implies the collect-and-collapse model of triggered star formation (Elmegreen & Lada 1977; Whitworth et al. 1994; Dale, Bonnell & Whitworth 2007). According to this model, the H II region is expanding into dense cloud and neutral material is accumulating in the shell between the shock and ionization fronts. The shell splits into massive clumps by large-scale instabilities, which develop along the shell. The clumps can be the sites of formation of the next generation of stars. Low-mass clumps can also be formed by small-scale gravitational instabilities (Deharveng et al. 2010). Shells consisting of massive clumps have been found on the periphery of several Galactic H II regions (e.g. Deharveng et al. 2003, 2008). The masses of dust clumps in the W40 ring are typical for low-mass cores. Nevertheless, their location along the ring is similar to what is expected in the collect-and-collapse mode. The presence of Class I and Class 0 sources associated with the ring clumps (Maury et al. 2011; Mallick et al. 2013) indicates that star formation is already taking place there.

A comparison of the morphologies of ionized gas and dust (Fig. 6, right panel) indicates that the ring is probably not associated with the main W40 H II region as the driving source (the massive star of the O9.5 spectral type associated with IRS 1A South, according to Shuping et al. 2012; see Fig. 6, large star) is located outside the area bounded by the ring. A likely source for the ring formation could be a distinct subregion of ionized gas associated with IRS 5, which is a massive star of the B1 V spectral type (Shuping et al. 2012; Mallick et al. 2013; see Fig. 6, small star) and lies to the north-west from IRS 1A South. The IRS 5 source is located within the area bounded by the ring but away from the geometrical centre of the ring closer to the western branch (Fig. 6, right panel). This could be a projection effect if the ring is not being viewed face-on. Using the maximum and minimum distances from IRS 5 to the inner boundary of the ring of ~ 3 arcmin (~ 0.44 pc) in the southern direction and of ~ 46 arcsec (~ 0.11 pc) to the west (Fig. 1), the inclination angle of the ring is $\sim 75°$ in the azimuthal plane, assuming it is circular in shape. The south-eastern part of the ring is probably closer to the observer.

7.2 Eastern branch of the ring

The VLA 3.6-cm and NIR sources are located close to the eastern branch of the dust ring. The area of dust clumps 2 and 3 has an elongated form in the north–south direction. The maps of ionized gas and dense molecular gas traced by CS(5–4) (Fig. 6) show similar shapes towards this area. The similarities imply that they belong to the same region where interaction between ionized and neutral material is taking place. There is an enhanced 2.12-μm H$_2$ emission region of a similar elongated form close to this part of the ring (Mallick et al. 2013), indicating the existence of shocked gas. We detected the narrow CH$_3$OH(2–1) line at ~ 8 km s^{-1} towards one of the eastern positions, confirming the existence of shocked gas or an inner YSO. The dust temperatures and molecular linewidths are higher in this area compared with the rest of the cloud. The CS(2–1) line profiles are asymmetric, implying contraction that is confirmed by model simulations (Section 5.3). The power-law indices of systematic velocity and density radial profiles in infalling gas derived from model simulations differ from those of the inside-out model of low-mass star formation, yet the estimate of the mass falling rate is typical for low-mass star formation regions. The model simulations also imply an existence of an extended low-density gas in this region. An ionized front from the main H II region or from the smaller region associated with VLA 3 probably expands into the cloud towards the west, where it is confronted with the dust ring. A shock wave is formed at the outer boundary of the eastern branch of the ring and compresses the material of the eastern clumps, probably forcing contraction.

7.3 Kinematics of the region

The gas kinematics is complex. Molecular lines at ~ 4.5–5 km s^{-1} are observed over the region. Towards the eastern branch of the dust ring, the CS and some other lines that can be associated with contracting gas are observed at ~ 7–8 km s^{-1}. The CO emission at higher velocities is observed to the east of the ring including the position of the main driving source. The strong and wide OH absorption line at ~ 7 km s^{-1}, observed towards the W40 H II region by Crutcher (1977), implies that the gas at this velocity is located in front of the H II region. Vallée (1987) and Shuping et al. (1999) concluded that there should be some gas located in front of the H II region. This foreground gas could give emission in molecular lines at ~ 7 km s^{-1} towards the eastern branch of the dust ring. The gas of the main cloud with ~ 4.5–5 km s^{-1} velocities is probably located at the background. Yet, the relative line-of-sight location of the gas at ~ 7–8 km s^{-1} and ~ 4.5–5 km s^{-1} is unclear towards the eastern branch of the ring, where two distinct CS(5–4) clumps with different velocities are associated with the dust ring.

7.4 Chemical composition

Molecular-line observations have revealed a large chemical differentiation over the cloud. The CS abundance in the contracting gas is ~ 7–10 times higher than in quiescent gas towards western positions and towards the dust clump 1. The CS enhancement could be connected with the evaporation of grain mantles, as predicted by hot core chemical models (e.g. Nomura & Millar 2004). An enhanced value of X(CS) is also derived towards the southern CS clump. This clump is not related to the ring, having a lower molecular hydrogen column density compared with the ring clumps. An absence of HCN and HCO$^+$ emission at the velocities of the infalling gas

($\sim$7–8 km s^{-1}) towards the eastern area and the detection of their rare isotopic lines at these velocities imply some specific excitation conditions. The reasons for this phenomenon could be connected with the absorption of optically thick lines in the extended low-density envelope, with an influence of continuum emission and/or with the conditions in the shocked gas on excitation of these molecules. However, the spectra are not of the good quality to perform detailed analysis.

The emission from nitrogen-bearing molecules (NH$_3$ and N$_2$H$^+$) is concentrated in clumps in the western branch of the dust ring. Towards the dust clump 6, the N$_2$H$^+$, NH$_3$ and H^{13}CO$^+$ lines are more narrow compared with the CS, HCN and HCO$^+$ lines. The latter do not trace clumps and probably arise in the surrounding gas with a higher degree of turbulence. In the other parts of the region, the NH$_3$ and N$_2$H$^+$ lines are weak and show no correlation with the ring structure. The NH$_3$ and N$_2$H$^+$ abundances towards the western positions are $\sim$3–10 times higher than towards the others (Table 8). The N$_2$H$^+$ abundance drop observed towards embedded massive YSOs (e.g. Pirogov et al. 2007; Zinchenko et al. 2009; Reiter et al. 2011) can be explained by N$_2$H$^+$ dissociative recombination. Low NH$_3$ and N$_2$H$^+$ abundances in the central and eastern parts of the W40 region can be associated with a high level of the ionized emission from the cluster stars and IRS 5, which penetrates through inhomogeneous surrounding gas, enhancing electron abundances and destroying nitrogen-bearing molecules or reducing their production rates.

7.5 Evolutionary status of the region

The eastern branch of the ring obviously has different conditions from the other parts of the cloud, which could be connected with different evolutionary stages. Class I sources are located near the eastern dust clumps 2 and 3, while Class 0 sources are close to the dust clumps 6 and 9 of the western branch (Maury et al. 2011). The NH$_3$ and N$_2$H$^+$ emission is concentrated mainly in the western branch, while the CS emission is high in the eastern part of the cloud. The eastern clumps 2 and 3 are more massive with a higher extent of non-thermal motions and higher dust temperatures. The CS line profiles towards them possess blue asymmetry. It is known that blue excess is more common for the UC H II regions than for their precursors (e.g. Fuller et al. 2005; Wu et al. 2007; Liu et al. 2011). We suggest that the eastern branch is more evolved than the western branch and an evolution sequence is going from east to west, from the eastern clumps that are more affected by the main driving source to the remote western clumps. Such an evolution sequence is seen in the surroundings of other massive stars (Liu et al. 2012). We suggest that the area of the eastern clumps 2 and 3 could probably be a site of triggered formation of the stars with masses higher than 1 M$_\odot$.

The questions that remain are connected with the detailed morphology of the gas with different velocities, especially towards the eastern branch of the dust ring. New multiline observations with high spatial resolution and sensitivity are needed to study in detail the structure of the region where interaction between ionized and neutral material is taking place. The modelling of chemical and physical parameters is needed to explain the reduced abundances of nitrogen-bearing molecules in the regions of enhanced ionization and anomalies in the HCN/H^{13}CN and HCO$^+$/H^{13}CO$^+$ intensity ratios in the gas with enhanced dynamical activity.

8 CONCLUSIONS

In order to study the structural and physical properties of dense molecular gas and dust associated with W40, which is one of the nearby H II regions, mm-wave molecular-line and 1.2-mm continuum single-dish observations have been performed. This region has been also observed using the GMRT interferometer at 1280 and 610 MHz. The cloud is located to the north-west of the main H II region and has a complex morphological and kinematical structure, including a clumpy dust ring and an extended dense core. It is thought that the ring is probably formed by the collect-and-collapse process because of the expansion of the smaller neighbouring H II region associated with IRS 5 and not being viewed face-on. The eastern branch of the ring is probably closer to us. The results of the study can be summarized as follows.

(i) Nine dust clumps in the ring have been deconvolved. Their sizes, masses and peak hydrogen column densities derived from the continuum data lie in the ranges $\sim$0.02–0.11 pc, $\sim$0.4–8.1 M$_\odot$ and $\sim$(2.5–11) $\times$ 10^{22} cm^{-2}, respectively. The strongest continuum emission comes from the eastern clumps 2 and 3.

(ii) Sharp differences in the morphologies of molecular and dust maps are found. Molecular lines at $\sim$4.5–5 km s^{-1} are observed over the whole region including the area without prominent dust emission. Towards the eastern branch of the ring, the CS and some other lines are observed at $\sim$7–8 km s^{-1}. The eastern dust clumps 2 and 3 are associated with the CS(5–4) clumps. NH$_3$, N$_2$H$^+$ and H^{13}CO$^+$ emission is enhanced towards the western dust clumps. The HCN(1–0) and HCO$^+$(1–0) maps show no correlation with dust. Probably, these lines and the CO lines (Zhu et al. 2006) trace the surrounding gas.

(iii) The physical parameters are derived from molecular-line data towards selected positions with a spatial extent of 40 arcsec, using LTE and non-LTE analysis. Ammonia kinetic temperatures are 21 and 16 K for two western clumps. Their virial masses, $\sim$3 M$_\odot$ and $\sim$2 M$_\odot$, respectively, are close to the masses derived from the dust continuum data. Number densities derived from the CS modelling lie in the range $\sim$(0.3–3.2) $\times$ 10^6 cm^{-3}. The CS(2–1) line profiles towards the eastern positions are self-reversed and asymmetric, implying infall motions. The calculations within the inhomogeneous non-LTE spherically symmetric model, with systematic velocity profile $\propto r^{-0.1}$, the density profile $\propto r^{-2}$ and an extended homogeneous low-density envelope, give good fits to the CS and C^{34}S profiles observed towards one selected position.

(iv) Molecular column densities and abundances imply strong chemical differentiation over the region. The CS abundances are enhanced towards the eastern dust clump 2 and the southern CS clump. The NH$_3$, N$_2$H$^+$, and H^{13}CO$^+$ abundances towards the western positions are up to an order of magnitude higher than towards the eastern positions. The electron abundances for two positions are $\sim$(2–3) $\times$ 10^{-7}. Probably, high X(e) values and low abundances of nitrogen-bearing molecules are related to inhomogeneous gas that surrounds the clumps.

(v) The area including the eastern clumps 2 and 3 differs from the western one. These clumps, which are associated with Class I sources, are more massive with a higher extent of non-thermal motions and higher dust temperatures. An interaction between ionized and neutral material is taking place in the vicinity of this area. Dense molecular gas is probably contracting. We suggest that the eastern branch of the ring is more evolved than the western branch and could probably be a site of triggered formation of stars with masses higher than 1 M$_\odot$.

REFERENCES

Bontemps S. et al., 2010, A&A, 518, L85
Caselli P., Walmsley C. M., Terzieva R., Herbst E., 1998, ApJ, 499, 234
Chen X., Shen Z-Q., Li J-J., Xu Y., He J-H., 2010, ApJ, 710, 150
Crutcher R. M., 1977, ApJ, 216, 308
Crutcher R. M., Chu Y. H., 1982, in Roger R. S., Dewdney P. E., eds, ASSL Vol. 93, Regions of Recent Star Formation. Reidel, Dordrecht, p. 53
Dale J. E., Bonnell I. A., Whitworth A. P., 2007, MNRAS, 375, 1291
Deharveng L., Lefloch B., Zavagno A., Caplan J., Whitworth A. P., Nadeau D., Martin S., 2003, A&A, 408, L25
Deharveng L., Lefloch B., Kurtz S., Nadeau D., Pomarés M., Caplan J., Zavagno A., 2008, A&A, 482, 585
Deharveng L. et al., 2010, A&A, 523, A6
Dobashi K., Uehara H., Kandori R., Sakurai T., Kaiden M., Umemoto T., Sato F., 2005, PASJ, 57, S1
Doty S. S., Leung C. M., 1994, ApJ, 424, 729
Elmegreen B. G., Lada C. J., 1977, ApJ, 214, 725
Evans N. J., II, 1999, ARA&A, 37, 311
Fuller G. A., Williams S. J., Sridharan T. K., 2005, A&A, 442, 949
Harju J., Walmsley C. M., Wouterloot J. G. A., 1993, A&AS, 98, 51
Klaassen P. D., Wilson C. D., 2007, ApJ, 663, 1092
Kuhn M. A., Getman K. V., Feigelson E. D., Reipurth B., Rodney S. A., Garmire G. P., 2010, ApJ, 725, 2485
Lee C. W., Myers P. C., Tafalla M., 2001, ApJS, 136, 703
Liu T., Wu Y-F., Liu S-Y., Qin S-L., Su Y-N., Chen H-R., Ren Z., 2011, ApJ, 730, 102
Liu T., Wu Y-F., Zhang H., Qin S-L., 2012, ApJ, 751, 68
Mallick K. K., Kumar M. S. N., Ojha D. K., Bachiller R., Samal M. R., Pirogov L., 2013, ApJ, preprint (arXiv:1309.7127)
Maury A. J., André P., Men'shchikov A., Könyves V., Bontemps S., 2011, A&A, 535, A77
Motte F., André P., Neri R., 1998, A&A, 336, 150

Myers P. C., Mardones D., Tafalla M., Williams J. P., Wilner D. J., 1996, ApJ, 465, L133
Nomura H., Millar T. J., 2004, A&A, 414, 409
Ossenkopf V., Henning T., 1994, A&A, 291, 943
Ott M., Witsel A., Quirrenbach A., Krichbaum T. P., Standke K. J., Schalinski C. J., Hummel C. A., 1994, A&A, 284, 331
Pirogov L., Zinchenko I., Lapinov A., Myshenko V., Shul'Ga V., 1995, A&AS, 109, 333
Pirogov L., Zinchenko I., Caselli P., Johansson L. E. B., Myers P. C., 2003, A&A, 405, 639
Pirogov L., Zinchenko I., Caselli P., Johansson L. E. B., 2007, A&A, 461, 523
Radhakrishnan V., Goss W. M., Murray J. D., Brooks J. W., 1972, ApJS, 24, 49
Reifenstein E. C., Wilson T. L., Burke B. F., Mezger P. G., Altenhoff W. J., 1970, A&A, 4, 357
Reiter M., Shirley Y. L., Wu J., Brogan C., Wootten A., Tatematsu K., 2011, ApJS, 195, 1
Rodney S. A., Reipurth B., 2008, in Reipurth B., ed., Handbook of Star Forming Regions, Vol. II. Astron. Soc. Pac., San Francisco, p. 683
Rodríguez L. F., Rodney S. A., Reipurth B., 2010, AJ, 140, 968
Sharpless S., 1959, ApJS, 4, 257
Shu F. H., 1977, ApJ, 214, 488
Shuping R. Y., Snow T. P., Crutcher R., Lutz B. L., 1999, ApJ, 520, 149
Shuping R. Y., Vacca W. D., Kassis M., Yu K. C., 2012, AJ, 144, 116
Smith J., Bentley A., Castelaz M., Gehrz R. D., Grasdalen G. L., Hackwell J. A., 1985, ApJ, 291, 571
Sohn J., Lee C. W., Park Y-S., Lee H. M., Myers P. C., Lee Y., 2007, ApJ, 664, 928
Swarup G., Ananthakrishnan S., Kapahi V. K., Rao A. P., Subrahmanya C. R., Kulkarni V. K., 1991, Current Science, 60, 95
Tafalla M., Myers P. C., Caselli P., Walmsley C. M., 2004, ApJ, 416, 191
Turner B. E., 1995, ApJ, 449, 635
Turner B. E., Chan K., Green S., Lubowich D. A., 1992, ApJ, 399, 114
Turner B. E., Pirogov L., Minh Y. C., 1997, ApJ, 483, 235
Vallée J. P., 1987, A&A, 178, 237
Vallée J. P., MacLeod J. M., 1991, A&A, 250, 143
Vallée J. P., Guilloteau S., MacLeod J. M., 1992, A&A, 266, 520
Van der Tak F. F. S., Black J. H., Schöier F. L., Jansen D. J., van Dishoeck E. F., 2007, A&A, 468, 627
Westerhout G., 1958, Bull. Astron. Inst. Netherlands, 14, 215
Whitworth A. P., Bhattal A. S., Chapman S. J., Disney M. J., Turner J. A., 1994, MNRAS, 268, 291
Wu Y-F., Henkel C., Xue R., Guan X., Miller M., 2007, ApJ, 669, L37
Zeilik M., Lada C. J., 1978, ApJ, 222, 896
Zhu L., Wu Y-F., Wei Y., 2006, Chin. J. A&A, 6, 61
Zinchenko I., Caselli P., Pirogov L., 2009, MNRAS, 395, 2234
Zinnecker H., Yorke H. W., 2007, ARA&A, 45, 481

This paper has been typeset from a TEX/LATEX file prepared by the author.